Journal of Applied Research and Technology

www.jart.icat.unam.mx

Journal of Applied Research and Technology 23 (2025) 178-191

Original

One-dimensional six-flux model (SFM-1D) for the description, estimation, and optimization of the radiant field in annular and tubular photocatalytic reactors

C. Nchikou

[a]*Universidad Autónoma de Nuevo León, UANL, Facultad de Ciencias Químicas, Av. Universidad s/n, Cd. Universitaria, C.P. 6645, San Nicolás de Los Garza, Nuevo León, México*
[b]*Universidad Tecnológica Bilingüe Franco Mexicana de Nuevo León Av. Paseo de San Juan No. 1000 Col. Mirador de San Antonio, C.P. 67255, Juárez, Nuevo León.*

Received 05 14 2024; accepted 10 11 2024
Available 04 30 2025

Abstract: The objective of this study was to solve the radiative transfer equation in one dimension using the six-flux model (SFM-1D) to characterize, estimate, and optimize the radiant field in annular photocatalytic reactors by performing an energy balance on a cylindrical element. The local volumetric rate of photon absorption ($LVRPA$), a critical parameter for describing photocatalytic reaction kinetics, was determined. This parameter was evaluated for two types of reactors: one with a constant-intensity radiant source positioned vertically at the center (annular reactor R1) and another with the source located externally around the reactor (tubular reactor R2). Simulations were conducted using the commercial TiO_2 P25 as the catalyst model, with its optical properties obtained from the literature. The model was assessed using the Heyney-Greenstein (HG) and diffuse reflectance (DR) phase functions. For reactor R1, the $LVRPA$ decreases from the reactor's inner wall to its outer wall, whereas for reactor R2, it decreases from the reactor wall toward its center. The volumetric rate of photon absorption per unit reactor length ($VRPA/H$), which provides a broader perspective on radiation absorption within the reactor, was established. The originality of the present model lies in its derivation from an energy balance, unlike existing models in the literature, which are based solely on the $LVRPA$ formulated for slab geometry using the SFM approach. The $VRPA$ calculated in this work differed by approximately 13.78% from values reported in the literature for reactor R1. For both reactors, $VRPA/H$ was found to increase exponentially with increasing catalyst loading (C_{cat}) until reaching a plateau where further increases became negligible. The optimal apparent thicknesses were approximately 4.8 and 10.6 for reactors R1 and R2, respectively, using the Heyney-Greenstein phase function. For R2, the optimal reactor radius was determined to be in the range of 1–3 cm, while the optimal reaction space thickness was less than 3 cm. Additionally, the dimensionless parameter η, introduced for optimization, was found to range between 0.55 and 0.8.

Keywords: Six-flux model, $LVRPA$, photocatalytic annular and tubular reactors.

*Corresponding author.
E-mail address: clovis.nchikou@uanl.edu.mx (C. Nchikou).
Peer Review under the responsibility of Universidad Nacional Autónoma de México.

1. Introduction

Modeling the radiant field in heterogeneous photocatalysis processes remains a challenging task due to the need to solve the radiative transfer equation (RTE) in its integro-differential form, which makes it very difficult to solve (Illi et al., 2019). Eq. (1) represents the steady-state and non-temperature-dependence of the RTE, which describes the different phenomena that occur on the light when it traverses a medium, such as absorption, in-scattering, and out-scattering, as represented in Eq. (1).

$$\frac{dI_\lambda(S,\Omega)}{ds} = -KI_\lambda(S,\Omega) - \sigma_\lambda I_\lambda(S,\Omega) + \frac{\sigma_\lambda}{4\pi}\int_{\Omega=4\pi} P(\Omega'\rightarrow\Omega)I_\lambda(S,\Omega')d\Omega' \quad (1)$$

where I_λ is the photon irradiance (W/m^2), K_λ the absorption coefficient (m^2/kg), σ_λ the scattering coefficient (m^2/kg), $P(\Omega'\rightarrow\Omega)$the scattering phase function, λ the wavelength (m), S the spatial coordinate (m) and Ω the directional solid angle (Steradian) (Fujii et al., 2022; Ghafoori et al., 2020; Howell et al., 2021).

The RTE gives an account of how light is dispersed or absorbed within a specific medium. Numerous numerical techniques, such as the discrete ordinates methods (DOM) and the Monte Carlo model, were employed to solve the RTE; nevertheless, these methods are time-consuming and need significant processing resources (Acosta-Herazo et al., 2020; Moreno-SanSegundo et al., 2020; Moreira & Li Puma, 2021). Another point to highlight is that many commercial software packages are not affordable to everyone. Solving the RTE allows for the determination of the $LVRPA$, one of the key parameters in the intrinsic kinetic rate equation of photocatalytic processes (Colina-Márquez et al., 2015). Simplified analytical methods for solving the RTE are often used because they provide a good balance between accuracy and computational efficiency. The six-flux model (SFM) has been proposed as an alternative simplified analytical method to solve the RTE and has been used successfully to describe the radiant field in photocatalytic reactors with different geometries (Brucato et al., 2006; Colina-Márquez et al., 2010; Nchikou et al., 2021; Moreira & Li Puma, 2021). The SFM stipulates that a photon after colliding with a particle can be scattered in six directions (Brucato et al., 2006). Li Puma et al. (2004), (Grčić & Li Puma, 2013) used the SFM in one dimension (SFM-1D) to find the $LVRPA$ on a slab geometry and then extended its expression to annular photocatalytic reactors (reactor R1) without performing an energy balance (Eq. (2)). This extension was made by replacing the x coordinate with the radial one (r), and by adding the term $\frac{\eta_0 R_2}{r}$ to take into account the attenuation of the photon flux with radial distance (Li Puma et al., 2004).

$$LVRPA_{ext} = \frac{I_0\left(\left(\omega_{corr}-1+\sqrt{1-(\omega_{corr})^2}\right)e^{-\frac{r}{\lambda\omega_{corr}}+\gamma} \left(\omega_{corr}-1-\sqrt{1-(\omega_{corr})^2}\right)e^{\frac{r}{\lambda\omega_{corr}}}\right)\eta_0 R_2}{\lambda_{\omega_{corr}}\omega_{corr}(1-\gamma)r} \quad (2)$$

where I_0 is the incident radiation intensity, f, b, and s are scattering probabilities (forward, backward, and sidewards, respectively), ω is the scattering albedo, η_0 is the ratio of the inner to the outer radius of the reactor, and R_2 is the reactor's outer radius.

$$a^* = 1-\omega f - \frac{4\omega^2 s^2}{(1-\omega f-\omega b-2\omega s)} \quad (3)$$

$$b^* = \omega b + \frac{4\omega^2 s^2}{(1-\omega f-\omega b-2\omega s)} \quad (4)$$

$$\omega_{corr} = \frac{b^*}{a^*} \quad (5)$$

$$\lambda_{\omega_{corr}} = \frac{1}{a^*(\sigma^*+\kappa^*)c_{cat}\sqrt{1-(\omega_{corr})^2}} \quad (6)$$

$$\gamma = \frac{1-\sqrt{1-(\omega_{corr})^2}}{1+\sqrt{1-(\omega_{corr})^2}}e^{-2\tau_{app}} \quad (7)$$

Nevertheless, avoiding using an energy balance to solve the RTE could affect the accuracy of the solution found. Furthermore, this approach cannot be applied to reactors of type R2 (Fig 1b), as the $LVRPA$ expression diverges as the radial coordinate approaches zero. Therefore, an energy balance must be performed to derive the $LVRPA$ on both reactors using adequate boundary conditions.

The primary objective of this work was to use the SFM approach to solve the RTE in cylindrical coordinates in one dimension, considering only the radial coordinate. This approach was applied to model the radiant field in two types of photocatalytic reactors: one with a constant-intensity radiant source positioned vertically inside the reactor (annular reactor R1, Fig. 1a) and another with the source placed vertically outside and surrounding the reactor (tubular reactor R2, Fig. 1b). The same energy balance on a cylindrical element used by Nchikou et al. (2021) was implemented here. Simulations were made with data reported in the literature. The catalyst model used here was the commercial titanium dioxide P25, but this model can also be applied to any other type of catalyst. Diffuse reflectance (DR) and Heyney-Greenstein (HG) phase functions were implemented and the optimum catalyst loading, and reactor radius were found. The $LVRPA$ found here on reactor R1 was then compared to that adopted by Li Puma et al. (2004).

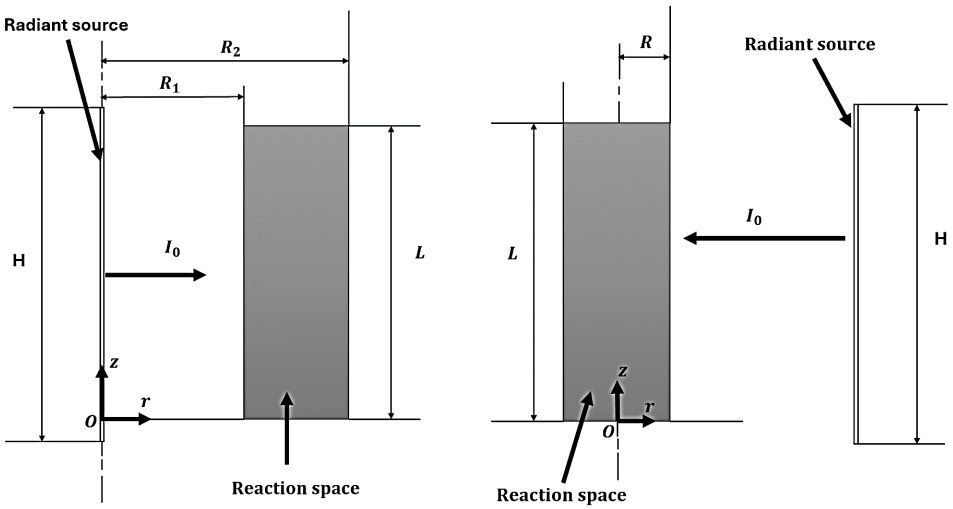

(a) (b)

Figure 1. Annular photocatalytic reactors of heights H.
a) Collimated radiant source of intensity I_0 and height L placed vertically at the reactor center.
b) Collimated radiant source of intensity I_0 and height L placed vertically outside and around the reactor.

2. Materials and methods

2.1. Mathematical modeling for the radiant field

2.1.1. Six-flux model in radial coordinate

For the derivation of the $LVRPA$ in polar coordinates, the novel SFM (SFM-1D) was formulated following the same steps used in the literature (Nchikou et al., 2021). As said before, the original SFM supposes that photons are scattered in any of the six principal directions with respect to the incoming radiation after colliding with a particle (Figure 1). Six different photon fluxes are defined, hence the name six-flux model (SFM).

In this work, an analytical expression of the $LVRPA$ was formulated by solving the RTE with the SFM approach in radial coordinate (SFM-1D) and performing the energy balance in a given control volume, as shown in Figure 3.

The SFM-1D used here relies on the following assumptions:

- Infinitely long annular or tubular photoreactor;
- Geometric optics holds (hence, large and largely spaced particles);
- Random particles distributed inside the space considered;
- The fluid can absorb any radiation;
- There is no emission by the heterogeneous system;
- When the photon hits a particle, only scattering or absorption occurs; the scattering probability is given by the catalyst albedo ω;
- The scattering event can occur only along the six directions of the cartesian coordinates, as presented in Figure 2;
- For symmetry considerations, the probability of scattering s along any of the four directions of the plane normal to the incoming direction is the same, the forward and backward probabilities f and b respectively are different according to Figure 2.

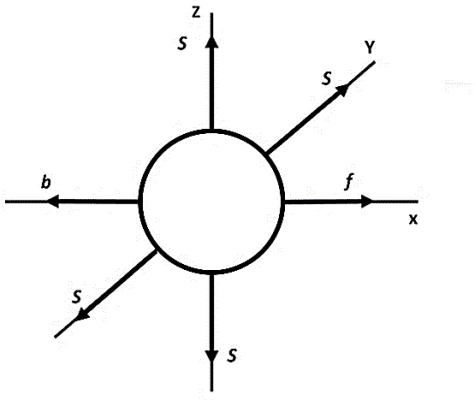

Figure 2. Six-flux model scattering directions.

$$r\partial\theta\partial z E_1|_{r+dr} = r\partial\theta\partial z E_1|_r - r\partial\theta\partial z E_1(1-\omega)n_p a_p \partial r - r\partial\theta\partial z E_1 \omega(b+4s)n_p a_p \partial r + r\partial\theta\partial z E_2 \omega(b) n_p a_p \partial r + \partial r\partial z E_3 \omega(s) n_p a_p r\partial\theta + \partial r\partial z E_4 \omega(s) n_p a_p r\partial\theta + r\partial r\partial\theta E_5 \omega(s) n_p a_p \partial z + r\partial r\partial\theta E_6 \omega(s) n_p a_p \partial z \quad (8)$$

out *in* *absorbed* *Scattering out* *Scattering in*

The photon balance in the volume of a cylinder, as shown in Figure 3 leads to:

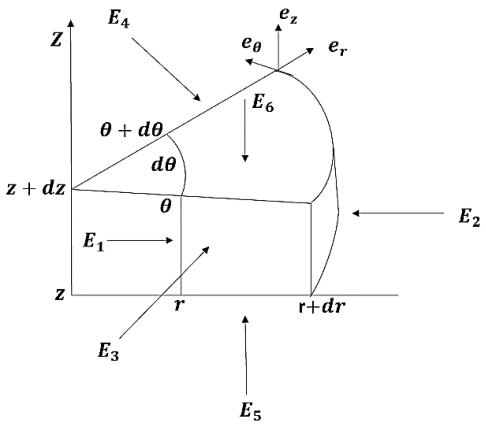

Figure 3. A differential model for the radiant energy balance.

where n_p is the number of particles per unit volume, a_p is the projected area of one particle, ω is the single albedo of the particle, f, b, and s are the forward, backward, and sidewise-scattering probabilities respectively which match Eq. (9).

$$f + b + 4s = 1 \quad (9)$$

Rearranging and dividing the Eq. (8) by $r\partial r\partial\theta\partial z$ and tending ∂r to zero, and performing the same way an energy balance in the other directions, one obtains the set of the following six equations:

$$\frac{\partial(rE_1)}{r\partial r} = \frac{1}{\lambda_0}[(-1+\omega f)E_1 + \omega b E_2 + \omega s(E_3+E_4+E_5+E_6)] \quad (10)$$

$$\frac{\partial(rE_2)}{r\partial r} = \frac{1}{\lambda_0}[(+1-\omega f)E_2 - \omega b E_1 - \omega s(E_3+E_4+E_5+E_6)] \quad (11)$$

$$\frac{\partial(E_3)}{r\partial\theta} = \frac{1}{\lambda_0}[(-1+\omega f)E_3 + \omega b E_4 + \omega s(E_1+E_2+E_5+E_6)] \quad (12)$$

$$\frac{\partial(E_4)}{r\partial\theta} = \frac{1}{\lambda_0}[(+1-\omega f)E_4 - \omega b E_3 - \omega s(E_1+E_2+E_5+E_6)] \quad (13)$$

$$\frac{\partial(E_5)}{\partial z} = \frac{1}{\lambda_0}[(-1+\omega f)E_5 + \omega b E_6 + \omega s(E_1+E_2+E_3+E_4)] \quad (14)$$

$$\frac{\partial(E_6)}{\partial z} = \frac{1}{\lambda_0}[(+1-\omega f)E_6 - \omega b E_5 - \omega s(E_1+E_2+E_3+E_4)] \quad (15)$$

where E_1, E_2, E_3, E_4, E_5, and E_6 represent the six discrete components of the specific radiation intensity (in this case E_2 is the incident beam, see Figure 1); f, b, and s represent the forward-scattering, backward-scattering, and sidewise-scattering probabilities, respectively. f, b, and s are calculated using an adequate phase function that accurately describes the catalyst particles' behavior, λ_0 is the photon mean free path. $\frac{1}{\lambda_0}$ is equal to $n_p a_p$ and also defined as $(\sigma^* + \kappa^*)c_{cat} + \kappa_c^* C_c$ where σ^* and κ^* are the catalyst-specific mass absorption and scattering coefficients respectively, κ_c^* is the specific mass absorption coefficient of a given contaminant, C_c is the contaminant concentration and C_{cat} is the catalyst loading. E_3, E_4, E_5, and E_6 are equal because of the symmetry consideration.

For symmetry consideration, the assumption of an infinitely large system results in:

$$\frac{\partial(E_5)}{\partial z} = \frac{\partial(E_6)}{\partial z} = 0 \quad (16)$$

Eq. (16) into (12-15) gives:

$$E_3 = E_4 = E_5 = E_6 = \frac{\omega s(E_1+E_2)}{1-\omega f-\omega b-2\omega s} \quad (17)$$

Eq. (17) into (10-11) gives:

$$\frac{\partial(\overline{E_1})}{\partial r} = -\overline{AE_1} + \overline{BE_2} \quad (18)$$

$$\frac{\partial(\overline{E_2})}{\partial r} = -\overline{BE_1} + \overline{AE_2} \quad (19)$$

where,

$$\overline{E_1} = rE_1 \quad (20)$$

$$\overline{E_2} = rE_2 \quad (21)$$

$$\overline{A} = \frac{1}{\lambda_0}\left(1 - \omega f - \frac{4(\omega s)^2}{1-\omega f-\omega b-2\omega s}\right) \quad (22)$$

$$\overline{B} = \frac{1}{\lambda_0}\left(\omega b + \frac{4(\omega s)^2}{1-\omega f-\omega b-2\omega s}\right) \quad (23)$$

Differentiating Eq. (18) with respect to the radial coordinate implies:

$$\frac{\partial^2(\overline{E_1})}{\partial r^2} = \overline{A}\frac{\partial(\overline{E_1})}{\partial r} + \overline{B}\frac{\partial(\overline{E_2})}{\partial r} \quad (24)$$

Eq. (18) into (24) implies:

$$\frac{\partial^2(\overline{E_1})}{\partial r^2} = -\overline{A}\left(-\overline{AE_1} + \overline{BE_2}\right) + \overline{B}\frac{\partial(\overline{E_2})}{\partial r} \quad (25)$$

Eq. (18) leads to:

$$\overline{E_2} = \frac{1}{\overline{B}}\overline{E_1} + \frac{\overline{A}}{\overline{B}}\frac{\partial(\overline{E_1})}{\partial r} \quad (26)$$

Eqs. (19) and (26) into (25) give:

$$\frac{\partial^2(\overline{E_1})}{\partial r^2} = \left(\overline{A}^2 - \overline{B}^2\right)\overline{E_1} \quad (27)$$

The general solution for Eq. (25) when $\overline{A} > \overline{B}$ is:

$$\overline{E_1} = pe^{\overline{K}r} + qe^{-\overline{K}r} \quad (28)$$

where,

$$\overline{K} = \sqrt{\overline{A}^2 - \overline{B}^2} \quad (29)$$

p and q are real constants.
Eq. (28) into (26) gives:

$$\overline{E_2} = p\frac{\overline{A}+\overline{K}}{\overline{B}}e^{\overline{K}r} + q\frac{\overline{A}-\overline{K}}{\overline{B}}e^{-\overline{K}r} \quad (30)$$

Eqs. (20-21, 28-30) give:

$$E_1 = \frac{1}{r}\left(pe^{\overline{K}r} + qe^{-\overline{K}r}\right) \quad (31)$$

and:

$$E_2 = \frac{1}{r}\left(p\frac{\overline{A}+\overline{K}}{\overline{B}}e^{\overline{K}r} + q\frac{\overline{A}-\overline{K}}{\overline{B}}e^{-\overline{K}r}\right) \quad (32)$$

The specific intensity of the radiation G is equal to $\sum_{i=1}^{6} E_i$ which leads to:

$$G(r,z) = \frac{1+4\zeta}{r}\left(p\left(1+\frac{\overline{A}+\overline{K}}{\overline{B}}\right)e^{\overline{K}r} + q\left(1+\frac{\overline{A}-\overline{K}}{\overline{B}}\right)e^{-\overline{K}r}\right) \quad (33)$$

where the parameter ζ is equal to $\frac{\omega s}{1-\omega f-\omega b-2\omega s}$. The $LVRPA$ will be defined as:

$$LVRPA(r,z) = (\kappa + \kappa_c)G(r,z) \quad (34)$$

where κ and κ_c are the catalyst and contaminant absorption coefficients respectively.

The volumetric rate of photon absorption per unit reactor length ($VRPA/H$), which describes the distribution of photon absorption within the reactor, provides a broader perspective on energy absorption as it is independent of the reactor length; it is defined later in this work and obtained by integrating the $LVRPA$ over the circular cross-section of the reactor. The overall volumetric rate of photon absorption ($OVRPA$) is obtained just by multiplying the $VRPA/H$ by the reactor length.

2.1.2. Modeling of the radiation absorption on reactor R2 (tubular reactor)

In this case, the fact that G should not diverge when $r = 0$ leads to:

$$p\left(1+\frac{\overline{A}+\overline{K}}{\overline{B}}\right) + q\left(1+\frac{\overline{A}-\overline{K}}{\overline{B}}\right) = 0 \quad (35)$$

which implies:

$$q = -p\frac{1+\frac{\overline{A}+\overline{K}}{\overline{B}}}{1+\frac{\overline{A}-\overline{K}}{\overline{B}}} \quad (36)$$

Combining Eqs. (33, 36) one finds the specific intensity of the radiation as:

$$G(r,z) = \frac{1+4\delta}{r}2p\left(1+\frac{\overline{A}+\overline{K}}{\overline{B}}\right)sh(\overline{K}r) \quad (37)$$

where:

$$\delta = \frac{\omega s}{(1-\omega f-\omega b-2\omega s)} \quad (38)$$

The boundary condition is:

$$E_2(R) = I_0 \quad (39)$$

where I_0 is the incident radiant flux reaching the reactor wall.

Eq. (32) into (39) implies:

$$\frac{1}{R}\left(p\frac{\overline{A}+\overline{K}}{\overline{B}}e^{\overline{K}R} + q\frac{\overline{A}-\overline{K}}{\overline{B}}e^{-\overline{K}R}\right) = \quad (40)$$

Eqs. (36, 40) give:

$$p = \frac{R\left(1+\frac{\overline{A}-\overline{K}}{\overline{B}}\right)}{\left(1+\frac{\overline{A}-\overline{K}}{\overline{B}}\right)\frac{\overline{A}+\overline{K}}{\overline{B}}e^{\overline{K}R} - \left(1+\frac{\overline{A}+\overline{K}}{\overline{B}}\right)\frac{\overline{A}-\overline{K}}{\overline{B}}e^{-\overline{K}R}} \quad (41)$$

Eqs. (37, 41) give the final expression of the specific intensity of the radiation as:

$$G(r,z) = \frac{sh(\overline{K}r)}{r} P_{R_{op}} I_0 \quad (42)$$

where:

$$P_{R_{op}} = \frac{2R\left(1+\frac{\overline{A}-\overline{K}}{\overline{B}}\right)\left(1+\frac{\overline{A}+\overline{K}}{\overline{B}}\right)(1+4\delta)}{\left(1+\frac{\overline{A}-\overline{K}}{\overline{B}}\right)\frac{\overline{A}+\overline{K}}{\overline{B}}e^{\overline{K}R} - \left(1+\frac{\overline{A}+\overline{K}}{\overline{B}}\right)\frac{\overline{A}-\overline{K}}{\overline{B}}e^{-\overline{K}R}} I_0 \quad (43)$$

The parameter $P_{R_{op}}$ depends on the reactor radius and catalyst's optical properties.

Finally, the volumetric rate of photon absorption per unit reactor length is found to be:

$$VRPA/H = \int_0^R \int_0^{2\pi} LVRPArdrd\theta = \frac{2\pi(ch(\overline{K}R)-1)}{\overline{K}} P_{R_{op}} I_0 \quad (44)$$

2.1.3. Modeling of the radiation absorption on reactor R1 (annular reactor)

In this case, one should apply the two following boundary conditions:

$$E_1(R_1,z) = G_0(R_1,z) \quad (45)$$

$$E_2(R_2,z) = 0 \quad (46)$$

This leads to solving Eqs. (47-48) simultaneously.

$$pe^{\overline{K}R_1} + \mathrm{q}e^{-\overline{K}R_1} = R_1 I_0 \quad (47)$$

$$p\frac{\overline{A}+\overline{K}}{\overline{B}}e^{\overline{K}R_2} + q\frac{\overline{A}-\overline{K}}{\overline{B}}e^{-\overline{K}R_2} = 0 \quad (48)$$

Eq. (48) leads to:

$$q = -p\frac{\overline{A}+\overline{K}}{\overline{A}-\overline{K}}e^{2\overline{K}R_2} \quad (49)$$

Eq. (49) into (47) gives:

$$p = \frac{(\overline{A}-\overline{K})e^{\overline{K}R_1}R_1}{(\overline{A}-\overline{K})e^{2\overline{K}R_1} - (\overline{A}+\overline{K})e^{2\overline{K}R_2}} I_0 \quad (50)$$

Eqs. (33, 49-50) give the final expression of the specific intensity of the radiation as:

$$G(r,z) = \frac{P_{R_{12op}}}{r}\left((\overline{A}-\overline{K})\left(1+\frac{\overline{A}+\overline{K}}{\overline{B}}\right)e^{\overline{K}(r-R_2)} - (\overline{A}+\overline{K})\left(1+\frac{\overline{A}-\overline{K}}{\overline{B}}\right)e^{\overline{K}(R_2-r)}\right) I_0 \quad (51)$$

$$P_{R_{12op}} = \frac{(1+4\delta)e^{\overline{K}(R_1+R_2)}R_1}{(\overline{A}-\overline{K})e^{2\overline{K}R_1} - (\overline{A}+\overline{K})e^{2\overline{K}R_2}} \quad (52)$$

The parameter $P_{R_{12op}}$ depends on the reactor's inner and outer radii as well as the catalyst's optical properties.

The volumetric rate of photon absorption per unit reactor length is found as:

$$VRPA/H = \int_{R_1}^{R_2}\int_0^{2\pi} LVRPArdrd\theta = \frac{2\pi\left((\overline{A}-\overline{K})\left(1+\frac{\overline{A}+\overline{K}}{\overline{B}}\right)\left(1-e^{\overline{K}(R_1-R_2)}\right) + (\overline{A}+\overline{K})\left(1+\frac{\overline{A}-\overline{K}}{\overline{B}}\right)\left(1-e^{\overline{K}(R_2-R_1)}\right)\right)P_{R_{12op}}I_0}{\overline{K}} \quad (53)$$

The optical thickness (τ) and the apparent optical thickness (τ_{app}) (Eqs. (54-55)) defined with the SFM approach (Colina-Márquez et al., 2010; Li Puma et al., 2004) were used in this work for optimization purposes.

$$\tau = (\sigma^* + \kappa^*)c_{cat}\epsilon \quad (54)$$

$$\tau_{app} = a^*\tau\sqrt{1-(\omega_{corr})^2} \quad (55)$$

where ϵ is the reactor thickness and can take the value $R_2 - R_1$ for reactor R1 and $2R$ for reactor R2.

3. Results: Simulations, comparisons, and discussions

Simulations were made by taking titanium dioxide as a catalyst model varying the catalyst loading. The HG and DR phase functions were used with $f = 0.754$, $b = 0.133$ and $s = 0.028$ for the HG phase function and $f = 0.11$, $b = 0.71$ and $s = 0.045$ for DR phase function. The characteristics of the catalyst and the reactor radius are defined in Table 1.

3.1. Absorption behavior inside both reactors

Figure 4 shows the absorption profiles for reactors R1 (Fig 4 d), e), and f) and R2 (Fig 4 a), b), and c). For R1, the $LVRPA$ decreases from the reactor's inner to its outer wall, while for R2, it decreases from the reactor wall to its center. The more the catalyst loading increases the more the $LVRPA$ increases in the reactors' zones close to the radiant source, while in the reactors' region far away from the radiant source, absorption decreases considerably.

Figure 5 displays the plot of the $LVRPA$ as a function of the reactor radius for both reactors for several catalyst loadings (0.1, 0.2, 0.3, 0.4, 0.5, and 0.6 g/L). For each catalyst loading, an exponential decay of the $LVRPA$ is observed, from the reactor wall towards the bottom in reactor R2 and from the inner to the outer wall in reactor R1. Additionally, the figure shows that for catalyst loadings below 0.3 g/L in both reactors, the energy absorption profile exhibits good uniformity. For higher catalyst loadings, the clouding effect begins to impede photons from penetrating the inner parts of the reactor. This observation is in good agreement with the literature (Alvarado-Rolon et al., 2018; Grčić & Li Puma, 2013; Li Puma et al., 2004; Nchikou et al., 2021). The clouding effect occurs due to the saturation of catalyst particles near the reactor wall, which prevents light from penetrating into the inner parts of the reactor (Colina-Márquez et al., 2010)

Table 1. Reactors and catalyst features.

R1 inner and outer radius: R_1 and R_2 (m)	0.013 and 0.019
R2 radius: R (m)	0.0165
The solar UV radiation flux: I_0 (W/m^2)	30
The specific mass absorption coefficient κ^* (m^2/kg)	174.75
The specific mass scattering coefficient σ^*(m^2/kg)	1295.75
The specific mass absorption coefficient of a given contaminant: κ_c^*	Considered here equal to zero.
The catalyst loading: C_{cat}(g/L)	Starting from zero g/L
The photon mean free path length: λ_0 (m)	$\frac{1}{\lambda_0} = (\sigma^* + \kappa^*)C_{cat} + \kappa_c^* C_c$
The scattering albedo ω: $\frac{\sigma^* C_{cat}}{(\sigma^*+\kappa^*)C_{cat}+\kappa_c^* C_c}$	0.88

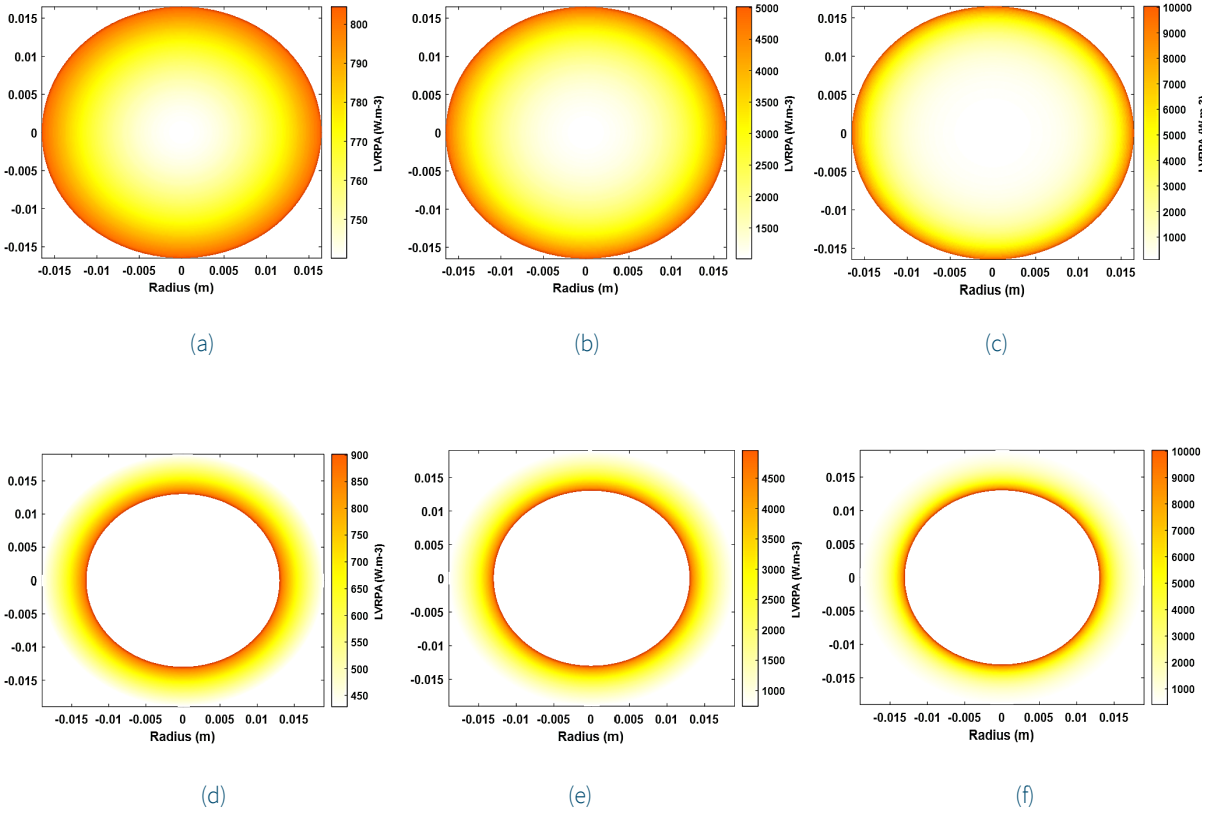

Figure 4. The $LVRPA$ profiles for different catalyst loadings for both reactors with Heyney-Greenstein phase function. a), b), and c) stand for R2 for 0.1, 0.5, and 1 g/L of Ccat respectively, and d), e), and f) stand for R1 for 0.1, 0.5, and 1 g/L of Ccat, respectively.

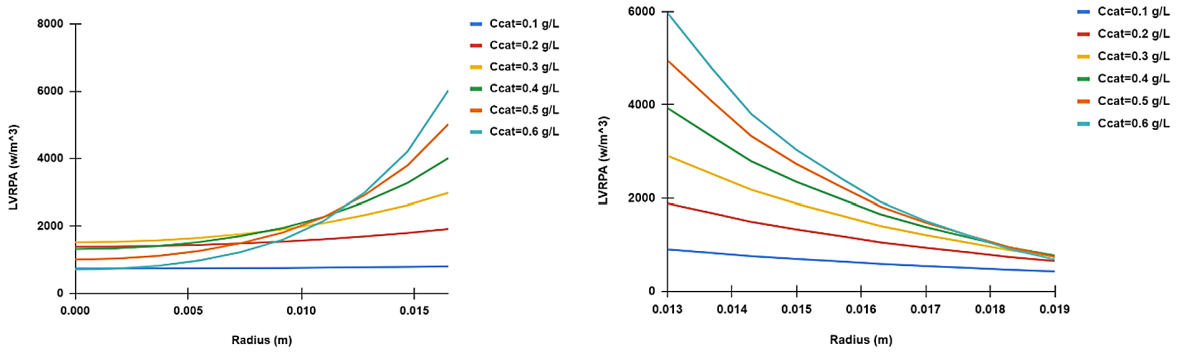

(a) (b)

Figure 5. The $LVRPA$ vs. radius plot for different catalyst loadings for both reactors with Heyney-Greenstein phase function: a) reactor R2; b) reactor R1.

3.2. Impact of the phase function on the radiation absorption for both reactors

The $LVRPA$ was simulated using diffuse reflectance (DR) and Henyey-Greenstein (HG) phase functions separately to illustrate the impact of phase function type on photon absorption and scattering in both photoreactors. The SFM-1D-DR and SFM-1D-HG represent the SFM-1D model with DR and HG phase functions, respectively. Figure 6 presents the $LVRPA$ for SFM-1D-DR and SFM-1D-HG as a function of the radial coordinate for each reactor at a catalyst loading of 0.3 g/L. The $LVRPA$ with SFM-1D-DR is lower than that with SFM-1D-HG throughout most of the reactors, except in the region very close to the radiant source. The preference of titanium dioxide particles for forward over backward scattering (Acosta-Herazo et al., 2016) explains this behavior, suggesting deeper photon penetration into the reactor's inner zone, which increases photon absorption with the HG phase function. In contrast, the DR phase function favors backward over forward scattering, resulting in lower photon penetration into the reactor's inner zone and, consequently, reduced photon absorption.

Figure 6 shows that absorption at the reactor wall using the DR phase function is higher than that using the HG phase function (Figs. 4, 7) because backward scattering is greater with the SFM-DR-1D than with the SFM-HG-1D. Specifically, for the DR phase function, the backward scattering probability is $b = 0.71$, which is more than six times higher than that for the HG phase function ($b = 0.113$) (Acosta-Herazo et al., 2016; Otálvaro-Marín et al., 2014).

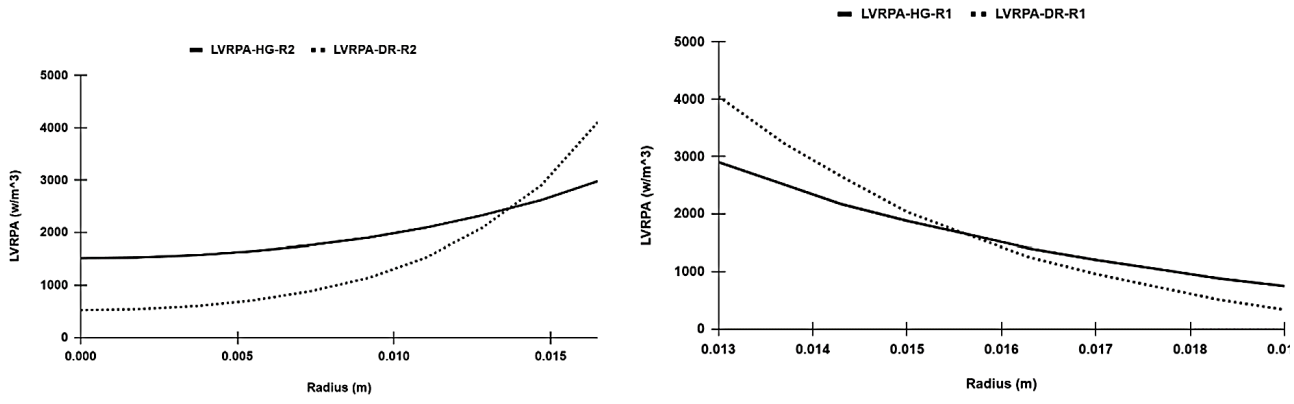

(a) (b)

Figure 6. The local volumetric rate of photon absorption vs. the reactor radius for both reactors at 0.3 g/l of catalyst loading with HG and DR phase functions: a) reactor R2; b) reactor R1.

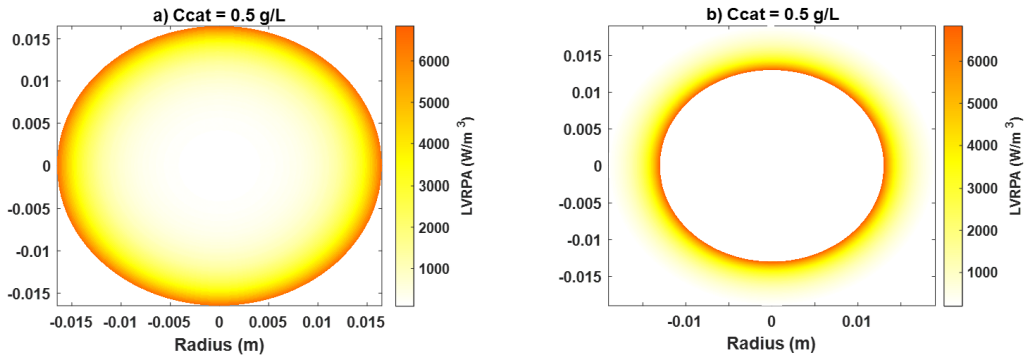

Figure 7. Local volumetric rate of photon absorption profile of both reactors at 0.5 g/l of catalyst loading with diffuse reflectance phase function: a) reactor R2; b) reactor R1.

3.3. The optimum catalyst loading, optical thickness, and apparent optical thickness for both reactors

The $VRPA/H$ which describes the distribution of the photon absorption inside the reactor gives a broader view of the energy absorption and was introduced for optimization purposes. Figure 8 shows how the $VRPA/H$ varies as a function of cataly st loading. The dashed and solid black lines represent the $VRPA/H$ for reactor R1 (R_1= 1.3 cm, R_2= 1.9 cm) using the model formulated in this work and the one adapted from the literature, respectively. Meanwhile, the solid red line represents the $VRPA/H$ for reactor R2 (R = 1.65 cm) using the model formulated in this work. In this figure, it is observed that the optimum value of the $VRPA/H$ is reached at 0.74 g/L of catalyst loading for R2, and at 1.85 g/L for R1, approximately. Above these values, the $VRPA/H$ remains almost constant, thus 0.74 g/L and 1.85 g/L of catalyst loading can be taken as the optimum catalyst loading for R2 and R1 respectively. The corresponding apparent optical thicknesses are respectively 10.59 and 4.8, approximately. These results are a little higher than those found by Nchikou et al. (2021), and Alvarado-Rolon et al. (2018) who worked respectively on a CPC reactor with sunlight and an annular photoreactor with artificial light with the characteristics of both reactors similar to those in this work and based on TiO_2. Alvarado-Rolon et al. (2018) worked with titanium dioxide optical properties different from those used in this work, and they used the Four-Flux model to find the $LVRPA$. It is then recommended to work at an apparent optical thickness between 0.71 and 10.59 with R2 and between 0.26 and 4.8 with R1 since working out of these intervals corresponds to either less production of oxidizing species (< 0.26 for R1 and < 1.43 for R2) or catalyst waste (> 4.8 for R1 and > 10.59 for R2). The recommended range for the apparent optical thickness for reactors of type R1 reported in the literature using the adapted model was 1.8-3.4 (Li Puma, 2005). Colina-Márquez et al. (2010) found the optimum apparent thickness of about 12.97 on tubular reactors using sunlight, a little higher than that found in this work (10.6), but the SFM they used was not too accurate.

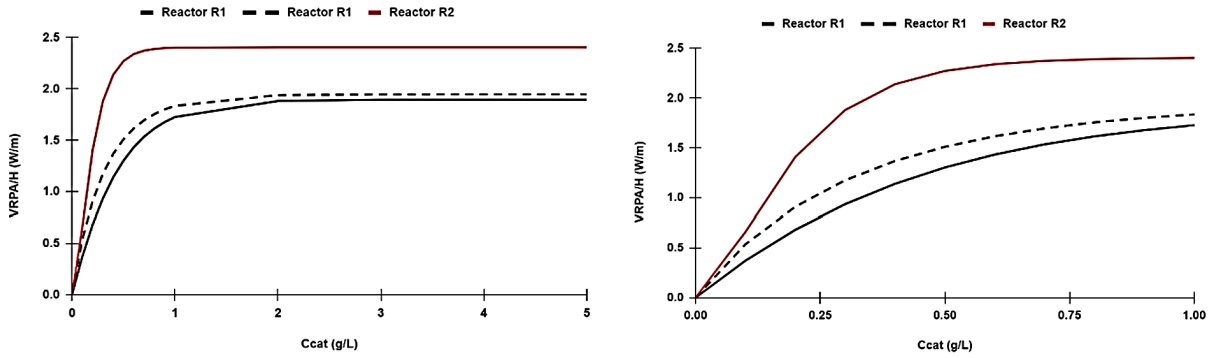

Figure 8. The $VRPA/H$ vs. catalyst loading plot for both reactors with Heyney-Greenstein phase function. a) From 0 to 5 g/L, b) From 0 to 1 g/L. The solid and dotted black lines represent the model formulated in this work and the one adapted for reactor R1, respectively.

Table 2 displays the optimum catalyst loading, apparent optical thickness, and optical thickness for different reactor radii. It was found that reactors of type R1, with the same reaction space (R_2-R_1), operate at the same optimum catalyst loading, and that the optimum catalyst loading decreases with an increase in the reaction space for both reactor types.

The findings in Table 2 show that τ_{op} and $\tau_{app,op}$ do not vary when changing the reactor radius for both reactor types. Therefore, the optical thickness and apparent optical thickness stand as dimensionless optimization parameters, both remove the dependence of the optimum catalyst loading on reactor radius while the second also removes the dependence of the optimum loading on the catalyst optical properties as shown in Table 3. Table 3 displays the optimum optical thickness and apparent optical thickness for different catalyst albedos and scattering coefficients with a fixed specific mass absorption coefficient (κ^* = 174.75 m^2/kg).

A significant fluctuation was found in the optimum optical thickness, while the optimum apparent optical thickness remained almost unchanged. As a result, the perceived optical thickness is a more reliable optimization parameter than the optical thickness. The recommended apparent optical thicknesses that lead to the optimum operating conditions for reactors R1 and R2 are approximately 4.8 and 10.6, respectively. Colina-Márquez et al. (2010) found the optimum apparent optical thickness to be around 12.97 on a tubular reactor using solar light as the radiant source. The differences could be due to the fact that the $LVRPA$ used by these authors was adapted from the SFM derived in rectangular geometry and that the discretization technique that they implemented on the tubular reactor was not accurate. It was also observed that the optimum catalyst loading decreases with the increase of catalyst albedo, which implies a decrease in terms of photon absorption since photon absorption and catalyst loading vary the same way (Alvarado-Rolon et al., 2018; Nchikou et al., 2021). The reduction in the catalyst's absorption capacity due to an increase in catalyst albedo could explain this phenomenon.

3.4. Comparison between the model formulated in this work and that adapted on reactor R1

The model developed in this study for reactor R1 was compared to that adapted from the literature (Li Puma et al., 2004), and the comparison was made by estimating the $VRPA/H$ with both models using Heyney-Greenstein phase function. Regarding Figure 8, the $VRPA/H$ with the adapted model is higher than with the current model, even though both models show similar variation. The discrepancy between both models for catalyst loadings from 0 to 5 g/L is about 13.78 % using the root mean square percentage. Since the adapted model was formulated without performing an energy balance, it appears to simplify the RTE, leading to an overestimation of radiation absorption compared to the model formulated in this work. Therefore, the actual model is more reliable than the adapted one.

Table 2. Optimum catalyst loading (Ccat,op), optical thickness (τ_{op}), and apparent optical thickness ($\tau_{app,op}$) with catalyst properties in Table 1 with Heyney-Greenstein phase function.

R (cm)	Ccat,op (g/L)	τ_{op}	$\tau_{app,op}$	R_1 (cm)	R_2 (cm)	Ccat,op (g/L)	τ_{op}	$\tau_{app,op}$
1	1.224	36	10.59	1	2	1.11	16.31	4.8
1.65	0.742	36	10.59	2	3	1.11	16.31	4.8
2	0.612	36	10.59	1	3	0.55	16.31	4.8
3	0.408	36	10.59	2	4	0.55	16.31	4.8
4	0.306	36	10.59	1	4	0.37	16.31	4.8
5	0.245	36	10.59	1	5	0.28	16.31	4.8
6	0.204	36	10.59	1	6	0.22	16.31	4.8

Table 3. Optimum catalyst loading, optical thickness, and apparent optical thickness for both reactors (R = 1.65 cm, R_1 = 1 cm, R_2 = 1.9 cm) at different catalyst albedo with a fixed specific mass absorption coefficient (κ^* = 174.75 m^2/kg) with Heyney-Greenstein phase function.

	R1			R2		
ω	Ccat,op (g/L)	τ_{op}	$\tau_{app,op}$	Ccat,op (g/L)	τ_{op}	$\tau_{app,op}$
0.8	2.44	12.79	4.75	0.99	28.55	10.6
0.85	2.1	14.71	4.77	0.85	32.68	10.61
0.9	1.69	17.68	4.81	0.68	38.93	10.6

3.5. Optimum radius for reactor R2

Figure 9 shows the evaluation of $VRPA/H$ as a function of catalyst loading at various reactor radii. It was found that $VRPA/H$ increases with both reactor radius and catalyst loading. This can be explained by the fact that increasing the reactor radius enlarges the reaction volume, which in turn facilitates light penetration into the deeper regions of the reactor, enhancing the interaction between photons and catalyst particles. However, an excessive increase in reactor radius can either lengthen the photon path to reach the inner part of the reactor or reduce the amount of light reaching each catalyst particle, leading to a decrease in light absorption.

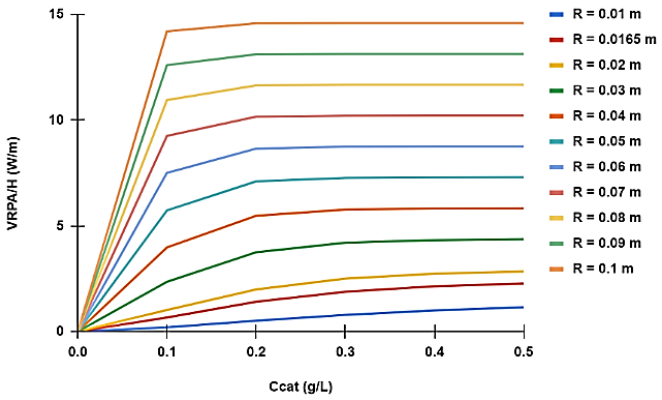

Figure 9. The $VRPA/H$ vs. catalyst loading plot for different reactor radii (R2) with Heyney-Greenstein phase function.

Increasing the catalyst loading leads to an increase in radiation absorption until a saturation point is reached. However, exceeding this limit may intensify competition for light absorption in zones near the reactor wall, preventing photons from penetrating into the reactor's inner regions. Therefore, it is crucial to balance the reactor radius and catalyst loading, as excessive increases in either parameter could result in economic losses or reduced process efficiency. Furthermore, it was observed that larger photoreactor radii corresponds to lower optimum catalyst loadings, while smaller photoreactor radii correspond to higher optimum catalyst loadings. This observation can be explained by the concepts of optical thickness and apparent optical thickness. A similar observation was made when working on CPC reactors (Fernández-Ibáñez et al., 1999). The optimum reactor radius that leads to the best operating conditions in reactor R2 taking into account what was discussed earlier should be chosen in such a way as to reduce the reactor zones where there is almost no absorption. For photoreactors with a high radius (greater than 3 cm), photons have difficulty reaching the inner part of the reactor. This is evident in Figure 10, where the $LVRPA$ is significantly lower at the reactor center compared to its value near the reactor wall. It is then useless to work with a high reactor radius (greater than 3 cm). For instance, with 0.2 g/L of catalyst loading and with the reactor radius equal to 3 cm, the $LVRPA$ at $r=\frac{R}{2}$ is about 50 % of its value at the zones near the reactor wall, and this percentage reduces considerably when the reactor radius increases (Fig 10). Reactors with small radii (less than 1) operate at very high catalyst loadings (Table 3). Under these conditions, the reaction space is too small, making photon penetration into the reactor volume more difficult, and the uniformity of radiation absorption is significantly reduced. It is recommended to work with reactors between 1 and 3 cm for optimization purposes. It has been found that the optimum diameter of compound parabolic reactors (CPC) reactor was between 2.5-5 cm (Dillert et al., 1999; Guillard et al., 1999) which is not far from that found in this work for reactors of types R2.

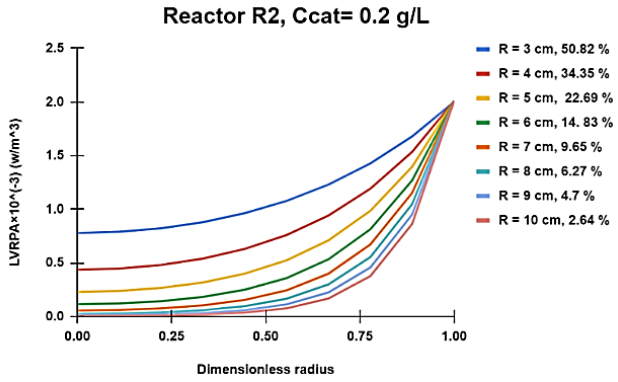

Figure 10. The $LVRPA$ versus dimensionless radius for different reactor radii and the ratio of the value of the $LVRPA$ at $r=\frac{R}{2}$ to its value at $r=R$ for reactor R2 with Heyney-Greenstein phase function.

3.6. Impact of the parameter $\eta = \frac{R_2}{R_2+\epsilon}$ on the photon absorption in the reactor R1

A dimensionless parameter η equal to $\frac{R_2}{R_2+\epsilon}$ where $\epsilon = R_2 - R_1$ is the reaction space thickness was introduced for optimization purpose. η lies between 0.5 and 1 but cannot take the values of 0.5 or 1, as these correspond to cases where the inner radius is zero or the inner and outer radii are equal, respectively. ϵ is very high when η is around 0.5 and very small when η is around 1. Figure 11 shows the plot of the $VRPA/H$ versus catalyst loading for two values of R_1 at different values of η. For every value of R_1, the $VRPA/H$ increases exponentially until reaching a maximum for each value of η (Figure 11 a and b). This $VRPA/H$ maximum is reached for a very small amount of catalyst when η is around 0.5 (ϵ very high) and for a very high amount of the catalyst loading when η tends to unity (ϵ very small). For η=0.55 the optimum value of the catalyst loading is around 0.3 g/L and 0.25 g/L for R_1=0.01 m and R_1=0.02 m, respectively (Fig 11). When η

approaches unity, ϵ becomes negligible compared to the outer reactor radius, and the reaction space width is very small. Conversely, when η approaches 0.5, the reaction space increases considerably. For instance, when R_1= 0.01 m, $\eta = 0.55$, and $\epsilon = 0.045$ m, while when R_1= 0.02 m, $\eta = 0.55$, and $\epsilon = 0.09$ m (Fig 11). In the latter case, the reaction space is too large, and photons will struggle to penetrate the reactor's inner zone. The inner radius of the reactor should be positioned close to the radiant source. The observations made regarding the optimization of reactors of type R2 can be extended to reactors of type R1 by comparing the reactor radius R to the reaction space ϵ. Thus, for any value of R_1, η should be chosen between 0.5 and 1 to ensure that the reaction space ϵ does not exceed 3 cm. For $\eta = 0.9$, reactor R1 is a very thin film reactor and the $VRPA/H$ increases very slowly, probably because the reaction space is very small ($\epsilon = 0.13$ cm for R_1= 0.01 m and $\epsilon = 0.25$ cm for R_1=0.02 m). In this case, the optimum catalyst loading is too high, the contact between photons and catalyst particles becomes difficult, and photon penetration into the reactor volume is hindered. The uniformity of radiation absorption is significantly reduced, negatively affecting the overall absorption.

It is then recommended to work with a value of η not too close to unity (less than 0.8). Many studies have been carried out with η between 0.55 and 0.8. Alvarado-Rolon et al. (2018) and Li Puma et al. (2003) worked with a reactor of type R1 with R_2= 0.025 m, η = 0.55 and R_2= 0.019 m, η = 0.76, respectively; meanwhile Moreira et al. (2010; 2011) used R_2= 0.044 m and η = 0.62.

4. Conclusion

By performing an energy balance on an element of a cylinder, the general solution of the radiative transfer equation (RTE) was derived in one dimension with respect to the radial coordinate using the SFM approach. The $LVRPA$ was formulated for two types of reactors: one with a constant-intensity radiant source located vertically at the center of the first reactor (reactor R1), and the other with the radiant source positioned outside the second reactor (reactor R2). The $LVRPA$ derived in this work differed from that formulated in the literature by approximately 13.78% for reactor R1, while for reactor R2, it was adjusted to avoid divergence at the reactor center. The present model successfully describes and optimizes radiation absorption in both reactors. Since it was derived from an energy balance, its originality makes it more reliable than that adapted from the literature. This model can be scaled up and applied to a variety of catalysts, not just the commercial titanium dioxide P25. The information provided here for the two types of photoreactors is significant, as it eliminates the need for statistical analysis of experimental designs and the use of complex models to solve the RTE, which typically require substantial time and financial resources. This approach could also be useful for developing a rate equation to describe the kinetics of photocatalytic degradation of various compounds. Future work will extend the formulation of the $LVRPA$ to 2D in reactors R1 and R2, considering variations in radiant source intensity along the z-axis.

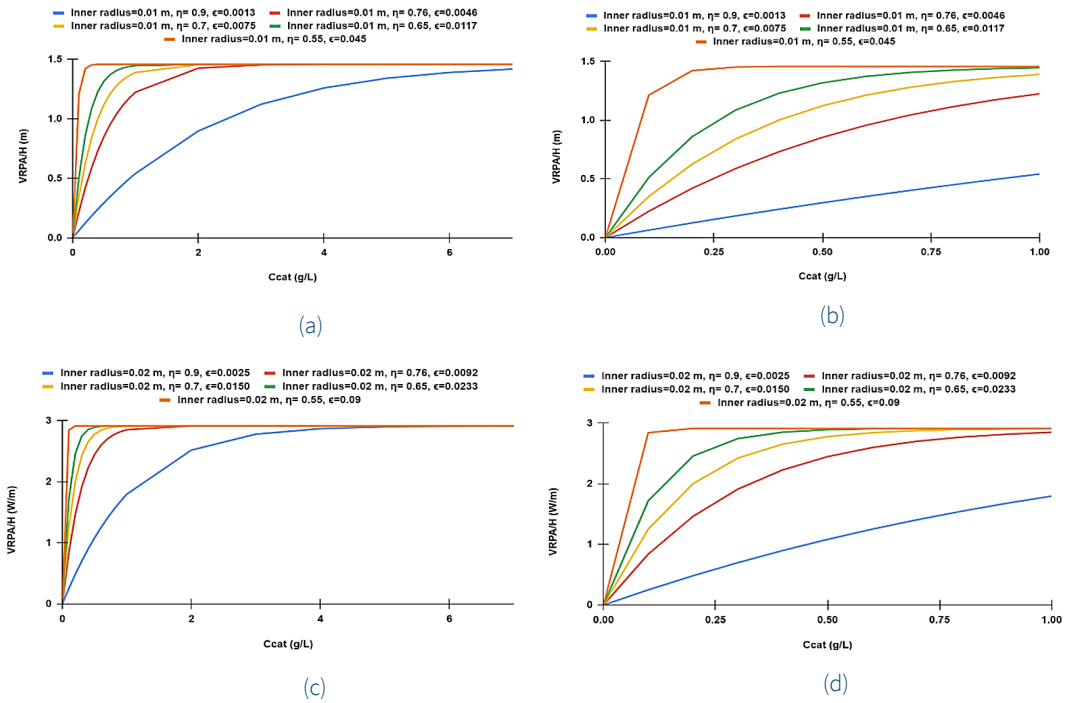

Figure 11. The $VRPA/H$ Vs catalyst loading plot for reactor R1 for different values of R_1 and η with Heyney-Greenstein phase function. a) From 0 to 7 g/L, R_1= 0.01 m, b) From 0 to 1 g/L, R_1= 0.01 m, c) From 0 to 7 g/L, R_1= 0.02 m, d) From 0 to 1 g/L, R_1= 0.02 m.

Conflict of interest

The author has no conflict of interest to declare.

Acknowledgment

Dr. Clovis Nchikou dedicates this article to Dr. Juan-Antonio Rojas-Estrada's memory.

Funding

The author did not receive any sponsorship to carry out the research reported in the present manuscript.

References

Acosta-Herazo, R., Cañaveral-Velásquez, B., Pérez-Giraldo, K., Mueses, M. A., Pinzón-Cárdenas, M. H., & Machuca-Martínez, F. (2020). A MATLAB-based application for modeling and simulation of solar slurry photocatalytic reactors for environmental applications. *Water*, *12*(8), 2196. https://doi.org/10.3390/w12082196

Acosta-Herazo, R., Monterroza-Romero, J., Mueses, M. Á., Machuca-Martínez, F., & Puma, G. L. (2016). Coupling the Six Flux Absorption–Scattering Model to the Henyey–Greenstein scattering phase function: Evaluation and optimization of radiation absorption in solar heterogeneous photoreactors. *Chemical Engineering Journal*, *302*, 86-96. https://doi.org/10.1016/j.cej.2016.04.127

Alvarado-Rolon, O. S. C. A. R., Natividad, R., Romero, R., Hurtado, L., & Ramírez-Serrano, A. R. M. A. N. D. O. (2018). Modelling and simulation of the radiant field in an annular heterogeneous photoreactor using a four-flux model. *International Journal of Photoenergy*, *2018*(1), 1678385. https://doi.org/10.1155/2018/1678385

Brucato, A., Cassano, A. E., Grisafi, F., Montante, G. I. U. S. E. P. P. I. N. A., Rizzuti, L., & Vella, G. (2006). Estimating radiant fields in flat heterogeneous photoreactors by the six-flux model. *AIChE journal*, *52*(11), 3882-3890. https://doi.org/10.1002/aic.10984

Colina-Márquez, J., Machuca-Martínez, F., & Puma, G. L. (2015). Modeling the photocatalytic mineralization in water of commercial formulation of estrogens 17-β estradiol (E2) and nomegestrol acetate in contraceptive pills in a solar powered compound parabolic collector. *Molecules*, *20*(7), 13354-13373. https://doi.org/10.3390/molecules200713354

Colina-Márquez, J., Machuca-Martínez, F., & Puma, G. L. (2010). Radiation absorption and optimization of solar photocatalytic reactors for environmental applications. *Environmental Science & Technology*, *44*(13), 5112-5120. https://doi.org/10.1021/es100130h

Dillert, R., Cassano, A. E., Goslich, R., & Bahnemann, D. (1999). Large scale studies in solar catalytic wastewater treatment. *Catalysis today*, *54*(2-3), 267-282. https://doi.org/10.1016/S0920-5861(99)00188-1

Fernández-Ibáñez, P., Malato, S., & De Las Nieves, F. J. (1999). Relationship between TiO2 particle size and reactor diameter in solar photoreactors efficiency. *Catalysis Today*, *54*(2-3), 195-204. https://doi.org/10.1016/S0920-5861(99)00182-0

Fujii, H., Terabayashi, I., Aoki, T., Inoue, Y., Na, H., Kobayashi, K., & Watanabe, M. (2022). Numerical study of near-infrared light propagation in aqueous alumina suspensions using the steady-state radiative transfer equation and dependent scattering theory. *Applied Sciences*, *12*(3), 1190. https://doi.org/10.3390/app12031190

Ghafoori, S., Nasirian, M., Al-Jamal, R., Mallouh, F. A., & Mehrvar, M. (2020). Statistical parameter optimization and modeling of photodegradation of methyl orange using a composite photocatalyst prepared by thermal synthesis. *Environmental Science and Pollution Research*, *27*, 45650-45660. https://doi.org/10.1007/s11356-020-10301-5

Grčić, I., & Li Puma, G. (2013). Photocatalytic degradation of water contaminants in multiple photoreactors and evaluation of reaction kinetic constants independent of photon absorption, irradiance, reactor geometry, and hydrodynamics. *Environmental science & technology*, *47*(23), 13702-13711. https://doi.org/10.1021/es403472e

Guillard, C., Disdier, J., Herrmann, J. M., Lehaut, C., Chopin, T., Malato, S., & Blanco, J. (1999). Comparison of various titania samples of industrial origin in the solar photocatalytic detoxification of water containing 4-chlorophenol. *Catalysis Today*, *54*(2-3), 217-228. https://doi.org/10.1016/S0920-5861(99)00184-4

Howell, J. R., Mengüç, M. P., Daun, K. J., & Siegel, R. (2021). *Thermal radiation heat transfer* (Seventh edition). CRC Press.
Howell, J. R., Mengüç, M. P., Daun, K., & Siegel, R. (2021). *Thermal radiation heat transfer*. CRC press. https://doi.org/10.1201/9780429327308

Illi, E., El Bouanani, F., Park, K. H., Ayoub, F., & Alouini, M. S. (2019). An improved accurate solver for the time-dependent RTE in underwater optical wireless communications. *IEEE Access*, *7*, 96478-96494.
https://doi.org/10.1109/ACCESS.2019.2929122

Li Puma, G. (2003). Modeling of thin-film slurry photocatalytic reactors affected by radiation scattering. *Environmental science & technology*, *37*(24), 5783-5791.
https://doi.org/10.1021/es0300362

Li Puma, G. (2005). Dimensionless analysis of photocatalytic reactors using suspended solid photocatalysts. *Chemical Engineering Research and Design*, *83*(7), 820-826.
https://doi.org/10.1205/cherd.04336

Li Puma, G., Khor, J. N., & Brucato, A. (2004). Modeling of an annular photocatalytic reactor for water purification: oxidation of pesticides. *Environmental science & technology*, *38*(13), 3737-3745.
https://doi.org/10.1021/es0301020

Moreira, J., Serrano, B., Ortiz, A., & de Lasa, H. (2010). Evaluation of photon absorption in an aqueous TiO2 slurry reactor using Monte Carlo simulations and macroscopic balance. *Industrial & engineering chemistry research*, *49*(21), 10524-10534.
https://doi.org/10.1021/ie100374f

Moreira, J., Serrano, B., Ortiz, A., & De Lasa, H. (2011). TiO2 absorption and scattering coefficients using Monte Carlo method and macroscopic balances in a photo-CREC unit. *Chemical engineering science*, *66*(23), 5813-5821.
https://doi.org/10.1016/j.ces.2011.07.040

Moreno-SanSegundo, J., Casado, C., & Marugan, J. (2020). Enhanced numerical simulation of photocatalytic reactors with an improved solver for the radiative transfer equation. *Chemical Engineering Journal*, *388*, 124183.
https://doi.org/10.1016/j.cej.2020.124183

Nchikou, C., Loredo-Medrano, J. Á., Hernández-Ramírez, A., Colina-Marquez, J. Á., & Mueses, M. Á. (2021). Estimation of the radiation field for CPC photocatalytic reactors using a novel six-flux model in two dimensions (SFM-2D). *Journal of Environmental Chemical Engineering*, *9*(6), 106392.
https://doi.org/10.1016/j.jece.2021.106392

Otálvaro-Marín, H. L., Mueses, M. A., & Machuca-Martínez, F. (2014). Boundary layer of photon absorption applied to heterogeneous photocatalytic solar flat plate reactor design. *International Journal of Photoenergy*, *2014*(1), 930439.
https://doi.org/10.1155/2014/930439

Moreira, R. P. M., & Puma, G. L. (2021). Multiphysics computational fluid-dynamics (CFD) modeling of annular photocatalytic reactors by the discrete ordinates method (DOM) and the six-flux model (SFM) and evaluation of the contaminant intrinsic kinetics constants. *Catalysis Today*, *361*, 77-84.
https://doi.org/10.1016/j.cattod.2020.01.012